Discovery of multi-anion antiperovskites X_6NFSn_2 (X = Ca, Sr) as promising thermoelectric materials by computational screening

Han, Dan; Zhu, Bonan; Cai, Zenghua; Spooner, Kieran B.; Rudel, Stefan S.; Schnick, Wolfgang; Bein, Thomas; Scanlon, David O.; Ebert, Hubert

DOI:
10.1016/j.matt.2023.10.022

Document Version
Publisher's PDF, also known as Version of record

Citation for published version (Harvard):
Han, D, Zhu, B, Cai, Z, Spooner, KB, Rudel, SS, Schnick, W, Bein, T, Scanlon, DO & Ebert, H 2024, 'Discovery of multi-anion antiperovskites X_6NFSn_2 (X = Ca, Sr) as promising thermoelectric materials by computational screening', *Matter*, vol. 7, no. 1, pp. 158-174. https://doi.org/10.1016/j.matt.2023.10.022

Matter

CellPress
OPEN ACCESS

Article

Discovery of multi-anion antiperovskites X_6NFSn_2 (X = Ca, Sr) as promising thermoelectric materials by computational screening

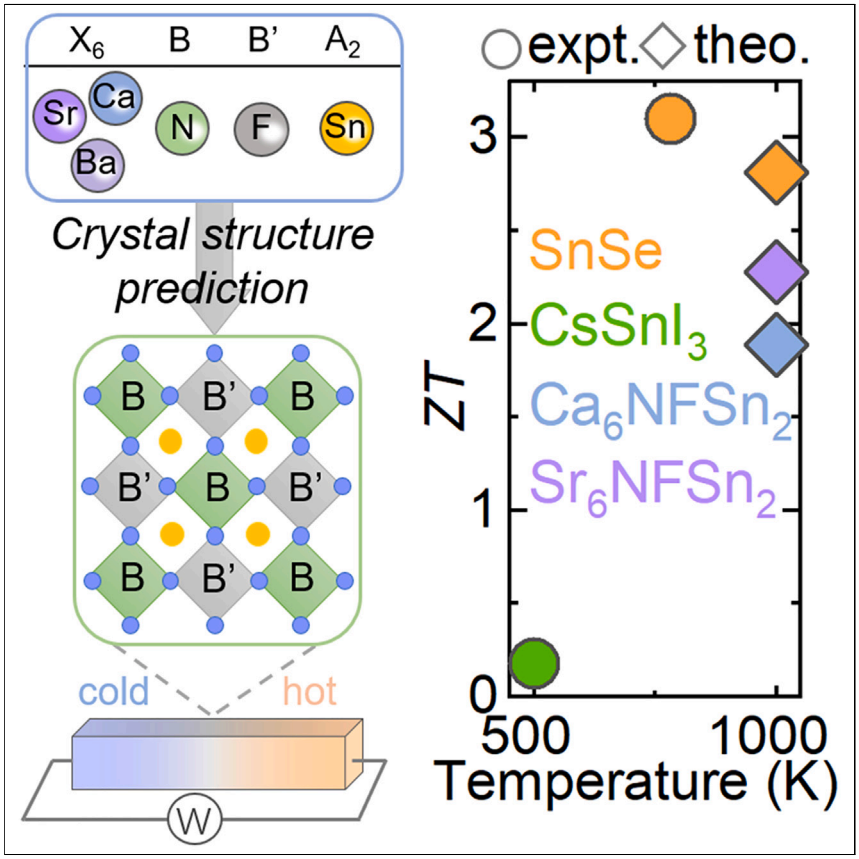

We design new multinary antiperovskites X_6NFSn_2 (X = Ca, Sr, Ba). By exploring the phase stability, electrical, and thermal properties, Ca_6NFSn_2 and Sr_6NFSn_2 are identified as promising thermoelectric materials.

Dan Han, Bonan Zhu, Zenghua Cai, ..., Thomas Bein, David O. Scanlon, Hubert Ebert

d.han@bham.ac.uk (D.H.)
d.o.scanlon@bham.ac.uk (D.O.S.)

Highlights

Designing phase-stable multi-anion antiperovskites X_6NFSn_2 (X = Ca, Sr, and Ba)

Identifying the promising thermoelectric properties of multi-anion antiperovskites

Extracting lattice thermal conductivity assisted by machine learning

Unraveling the origin of low lattice thermal conductivity of X_6NFSn_2 (X = Ca, Sr)

Discovery
A new material or phenomena

Han et al., Matter 7, 158–174
January 3, 2024
https://doi.org/10.1016/j.matt.2023.10.022

CellPress
OPEN ACCESS

Matter

Article

Discovery of multi-anion antiperovskites X_6NFSn_2 (X = Ca, Sr) as promising thermoelectric materials by computational screening

Dan Han,[1,2,3,5,6,*] Bonan Zhu,[2,5] Zenghua Cai,[4] Kieran B. Spooner,[2,3] Stefan S. Rudel,[1] Wolfgang Schnick,[1] Thomas Bein,[1] David O. Scanlon,[2,3,*] and Hubert Ebert[1]

SUMMARY

The thermoelectric performance of existing perovskites lags far behind that of state-of-the-art thermoelectric materials such as SnSe. Despite halide perovskites showing promising thermoelectric properties, namely, high Seebeck coefficients and ultralow thermal conductivities, their thermoelectric performance is significantly restricted by low electrical conductivities. Here, we explore new multi-anion antiperovskites X_6NFSn_2 (X = Ca, Sr, and Ba) via B-site anion mutation in antiperovskite and global structure searches and demonstrate their phase stability by first-principles calculations. Ca_6NFSn_2 and Sr_6NFSn_2 exhibit decent Seebeck coefficients and ultralow lattice thermal conductivities (<1 W m^{-1} K^{-1}). Notably, Ca_6NFSn_2 and Sr_6NFSn_2 show remarkably larger electrical conductivities compared to the halide perovskite $CsSnI_3$. The combined superior electrical and thermal properties of Ca_6NFSn_2 and Sr_6NFSn_2 lead to high thermoelectric figures of merit (ZTs) of ~1.9 and ~2.3 at high temperatures. Our exploration of multi-anion antiperovskites X_6NFSn_2 (X = Ca, Sr) realizes the "phonon-glass, electron-crystal" concept within the antiperovskite structure.

INTRODUCTION

Thermoelectric (TE) materials allow for a direct energy conversion between heat and electricity, and they have potential applications in heat pumping and solid-state power generators.[1–3] The conversion efficiency of TE materials can be assessed by the dimensionless figure of merit (ZT) $ZT = \frac{S^2\sigma}{\kappa_l+\kappa_e}T$. A combination of a large Seebeck coefficient (S), a high electrical conductivity (σ), and a low thermal conductivity (κ; sum of electronic conductivity [κ_e] and lattice thermal conductivity [LTC] [κ_l]) is highly desired for high-performance TE materials.[4] However, the complex interrelationship between electrical and thermal properties makes it challenging to achieve an ultrahigh ZT.[5] For decoupling electrical and thermal properties, the concept of "phonon-glass, electron-crystal" (PGEC), viz. designing TE materials in structures allowing for efficient transport of charge carriers, as in a good semiconductor crystal, and largely blocking thermal transmission by the lattice, as in a glass, has been proposed.[6] Indeed, the PGEC concept redirects the materials design strategy to intrinsic features of structure and bonding characteristics, and PGEC behavior was originally observed in cage-like compounds such as skutterudites and clathrates, where heavy atoms trapped in the cages "rattle" and thus strongly scatter phonons.[7–9] Besides skutterudites and clathrates, the perovskite structure provides a platform to validate the PGEC concept as the heavy-element or molecular group sits at the A site of the AMX_3 perovskite structure and forms a large cuboctahedral cage with 12 atoms at

PROGRESS AND POTENTIAL

The concept of "phonon-glass, electron-crystal" (PGEC) has been proposed to decouple electrical and thermal properties and thus to enhance the figure of merit (ZT) of thermoelectric (TE) materials. PGEC behavior was originally observed in cage-like compounds such as skutterudites and clathrates. In addition to skutterudites and clathrates, the perovskite structure provides a platform to validate the PGEC concept. Nevertheless, the thermoelectric performance of existing perovskites lags far behind that of the state-of-the-art thermoelectric materials such as SnSe. Here, we design multi-anion antiperovskites X_6NFSn_2 (X = Ca, Sr, and Ba). Ca_6NFSn_2 and Sr_6NFSn_2 exhibit superior electrical and thermal properties, leading to high ZTs of ~1.9 and ~2.3 at 1,000 K, which are higher than the reported perovskite oxides and halides. This design realizes the PGEC concept within the vast family of perovskite-related compounds and provides a new strategy for promising TE materials.

the X site. Additionally, the A and X interactions are normally ionic and weak, with large vibrational amplitudes for the cations, which provides a chance for A-site element rattling at their equilibrium positions.[10]

Oxide perovskites have a long history of being studied as TE materials because of their high-temperature air stability, environmental friendliness, and straightforward synthesis.[11] However, the main limitation of these perovskites is their high κ (>10 W m^{-1} K^{-1}).[11,12] State-of-the-art bulk TE materials like SnSe and PbTe exhibit κs of less than 3 W m^{-1} K^{-1} at the same temperature (300 K).[13] The well-studied $SrTiO_3$ perovskite with dopants La and Nb has shown promise in recent years and achieves a maximum *ZT* of 0.6 at over 1,000 K.[14] Nonetheless, it is much inferior to bulk TE materials such as SnSe, PbTe, and BiCuSeO and typical half-Heusler alloys with demonstrated *ZT*s >1 at high temperature in a laboratory setting.[15–18] Halide perovskites have drawn great attention with a view on application in photovoltaics, light-emitting diodes, and photodetectors due to their extraordinary optoelectronic properties.[19–23] Generally, metal halides are not seriously considered as TE materials. However, a large *S* combined with an ultralow κ have been claimed for both hybrid and all-inorganic halide perovskites,[24–26] which spurs the investigation of TE properties of halide perovskites.[27,28] Despite the inherent high *S* and the ultralow κ, it is reported that intended doping for increasing conductivity in $CH_3NH_3PbX_3$ (*X* = Cl, Br, I) and $CsPbX_3$ (*X* = Cl, Br, I) remains challenging, which is attributed to the defect-tolerant electronic structure and ionic compensation of charged point defects.[29–31] In contrast to the lead analogs, $CsSnX_3$ (*X* = Cl, Br, I) perovskites exhibit the possibility of using self-doping processes of Sn^{2+} to Sn^{4+} to achieve p-type electrical conductivities.[32,33] Nevertheless, the σ is still low and seriously limits its TE performance; that is, current maximum *ZT* values of 0.08 and 0.175 are attained in $CsSnI_3$ at room temperature (RT) and 500 K, respectively.[34,35]

In addition to perovskites, nitride and oxide antiperovskites have been investigated as TE materials.[36–40] Antiperovskites maintain the perovskite structure, while their ionic types are inverted.[41–45] Both nitride and oxide antiperovskites can show enhanced stability compared to halide perovskites. Similar to the cases of traditional binary nitrides,[46–48] nitride antiperovskites exhibit high κs, which are detrimental to the TE performance; for example, the κs of Sr_3AsN are larger than 10 W m^{-1} K^{-1} at RT.[36] Compared to nitride antiperovskites, oxide antiperovskites have lower κs, while they suffer from a low *S* due to narrower band gaps.[37,38] Some of them (Ba_3OGe, X_3OSn, and X_3OPb [*X* = Ca, Sr, Ba]) even show band-gap closing, which is unfavorable for high-performance TE materials due to the cancellation of the electron and hole carrier transport and the loss of the n- or p-type character.[37] Thus far, many issues remain to be solved for realizing the full potential of existing perovskite-related materials for TE applications.

In light of the complex crystal structure with heavy elements favoring low LTC, here, we design multi-anion antiperovskites (double-antiperovskites) X_6NFSn_2 (*X* = Ca, Sr, and Ba), which can be regarded as the B-site anion mutation in antiperovskite X_3OSn (*X* = Ca, Sr, and Ba). Crystal structure predictions for X_6NFSn_2 (*X* = Ca, Sr, and Ba) are performed using *ab initio* random structure searching (AIRSS) and particle swarm optimization.[49–52] All of the low-energy structures of X_6NFSn_2 (*X* = Ca, Sr, and Ba) appear in antiperovskite structures. Based on first-principles calculations, we demonstrate the phase stabilities, including dynamic stability and thermodynamic stability, and investigate the electronic structure of Ca_6NFSn_2 (space group [SG] $Fm\bar{3}m$), Sr_6NFSn_2 (SG $R\bar{3}$), and Ba_6NFSn_2 (SG $R\bar{3}$). The electrical and TE properties of Ca_6NFSn_2 and Sr_6NFSn_2 are further studied because of their larger band gaps

[1]Department of Chemistry and Center for NanoScience (CeNS), University of Munich (LMU), 81377 Munich, Germany

[2]Department of Chemistry, University College London, London WC1H 0AJ, UK

[3]School of Chemistry, University of Birmingham, Birmingham B15 2TT, UK

[4]Jiangsu Key Laboratory of Micro and Nano Heat Fluid Flow Technology and Energy Application, School of Physical Science and Technology, Suzhou University of Science and Technology, Suzhou 215009, China

[5]These authors contributed equally

[6]Lead contact

*Correspondence: d.han@bham.ac.uk (D.H.), d.o.scanlon@bham.ac.uk (D.O.S.)

https://doi.org/10.1016/j.matt.2023.10.022

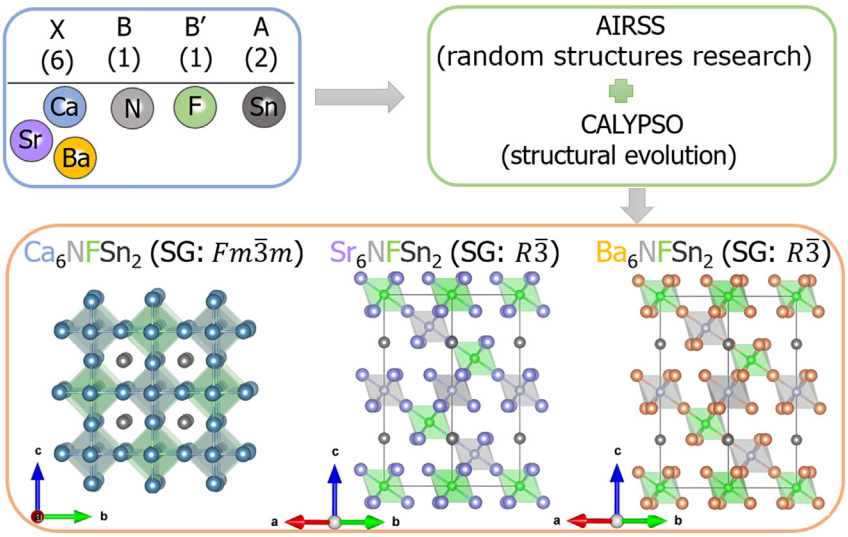

Figure 1. A schematic diagram of the crystal structure prediction of X_6NFSn_2 (X = Ca, Sr, and Ba)
Conventional cells of compounds are displayed. Corresponding space group (SG) are given in parentheses. Color codes are given in the formula of the compounds.

(>0.2 eV), which are essential for maintaining a single carrier type and therefore a high ZT at high temperature. Ca_6NFSn_2 and Sr_6NFSn_2 both display low LTCs and remarkably enhanced electrical conductivities compared to halide perovskites, thus resulting in the predicted high maximum ZTs of p-type Ca_6NFSn_2 (1.89) and Sr_6NFSn_2 (2.28) at 1,000 K. Notably, the extraction of high-order force constants (FCs) for computing the LTC is achieved by advanced machine learning algorithms and first-principles calculations, which avoids the extremely high cost for extracting high-order FCs via substantial computations for the compounds with lower symmetry and large unit cells.

RESULTS AND DISCUSSION

Crystal structure prediction

We performed global structure searches for X_6NFSn_2 (X = Ca, Sr, and Ba) to identify whether their low-energy structures can crystallize in the double-antiperovskite structure via AIRSS and crystal structure analysis by particle swarm optimization (CALYPSO). Using AIRSS, for X_6NFSn_2 (X = Ca, Sr, and Ba), 2,114, 2,078, and 2,075 random structures were generated, respectively, which were subsequently relaxed by CASTEP. As shown in Table S1, a low-energy structure with the symmetry of $Fm\bar{3}m$ of Ca_6NFSn_2 is found, which is identified by CALYPSO searching as well. Sr_6NFSn_2 and Ba_6NFSn_2 with the symmetry of $R\bar{3}$ exhibit the lowest energies. Explicit crystal parameters of these compounds are summarized in Table S2. Ca_6NFSn_2 (SG $Fm\bar{3}m$), Sr_6NFSn_2 (SG $R\bar{3}$), and Ba_6NFSn_2 (SG $R\bar{3}$) form a double-antiperovskite structure with X-site cations (X = Ca, Sr, and Ba) at the corners of the octahedra, B/B′-site anion (N/F) at the center of octahedra, and Sn located at the A site, as displayed in Figure 1. $[X^{2+}{}_6N^{3-}]$ and $[X^{2+}{}_6F^{-}]$ (X = Ca, Sr, and Ba) octahedra alternate along the three crystallographic axes and form the rock-salt-type ordering. Heavy-atom Sn at the A site forms cuboctahedral cages with 12 Ca, Sr, and Ba atoms at the X site, and the distances between them are larger than 3.48, 3.55, and 3.63 Å, respectively, providing a chance for Sn atoms to act as cage rattlers. As the X-site element becomes heavier from Ca to Sr or Ba, the crystal structure evolves from cubic to trigonal symmetry while maintaining the corner-sharing octahedra. In contrast to high-symmetry Ca_6NFSn_2 without distortion, Sr_6NFSn_2 and Ba_6NFSn_2 show

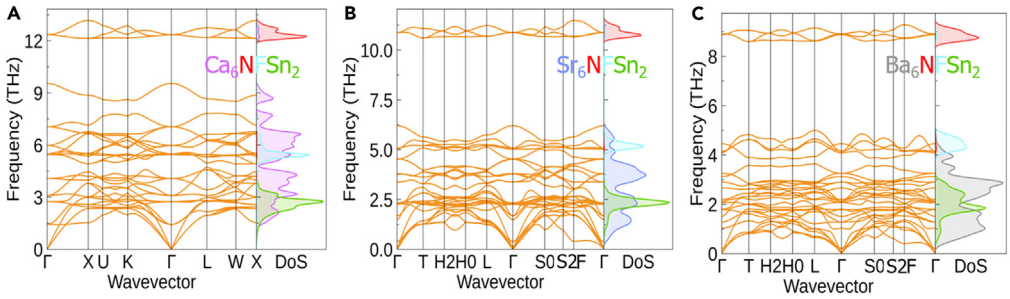

Figure 2. Phonon spectra together with atom-projected density of states (DoS) curves of X_6NFSn_2

(A–C) Phonon spectra together with atom-projected density of states (DoS) curves (A–C) of X_6NFSn_2 (X = Ca, Sr, Ba).

$a^-a^-a^-$ (Glazer's notation) octahedral tilting, which is consistent with observations in the oxide perovskites, i.e., when the X-site radius increases, the titling of octahedra can appear.[53,54] The phase stabilities of X_6NFSn_2 (X = Ca, Sr, and Ba) are evaluated in the next section.

Phase stability and electronic structure

The mechanical stability of X_6NFSn_2 (X = Ca, Sr, and Ba) is firstly evaluated. As summarized in Table S3, all compounds fulfill the Born-Huang stability criteria[55] and are mechanically stable. The thermodynamic stability of Ca_6NFSn_2, Sr_6NFSn_2, and Ba_6NFSn_2 was evaluated via convex hull analysis. All three compounds present on the hull, suggesting their thermodynamic stability. Via convex hull constructions, the predominant decomposition pathway of X_6NFSn_2 into corresponding binary and ternary materials is identified and is given in the supplemental information. Moreover, a stable polyhedron of Ca_6NFSn_2 in the phase diagram is identified (see Figure S1), and the chemical potential region limits are given in Table S4, which demonstrate its thermodynamic stability. All the reported competing phases from the Materials Project, OQMD, and ALFOW databases were considered for the phase diagram of Ca_6NFSn_2.[56–58] It is displayed as a representation because the phase diagram of multinary compounds calculated by hybrid functional is time consuming to create. With regard to experimental results, it is noteworthy that several alkaline-earth metal nitrohalide Ca_2NI and Ba_2NX (X = F, Cl, Br) samples were successfully prepared under high temperature (~1,000 K).[59–61] The precursors of antiperovskite Ca_3OSn samples were heated at 1,123 K for several hours and then quenched.[38] Analogous reactions might enable the synthesis of the herein suggested compounds.

After validating the thermodynamic stability, their dynamic stabilities were assessed via harmonic phonon calculations. Three compounds show dynamic stability, as indicated by the absence of imaginary phonon modes (Figures 2A–2C). Thus far, the phase stability of X_6NFSn_2 (X = Ca, Sr, Ba) has been demonstrated. According to the inverse relationship between the reduced mass and frequency, the high-frequency phonon modes in the three compounds are dominated by the motions of N, the mid-frequency ones mostly comprise the motions of alkaline-earth metal (Ca/Sr/Ba) and F atoms, and the low-frequency ones are contributed by the motions of Sn and alkaline-earth metal (Ca/Sr/Ba) atoms, as shown in Figures 2A–2C. Ba_6NFSn_2 displays the narrowest frequency range among the three compounds. It can be ascribed to the heavy X atoms downshifting the frequencies. The highest acoustic mode boundary frequencies of Ca_6NFSn_2, Sr_6NFSn_2, and Ba_6NFSn_2 are 3, 2.5, and 2 THz, respectively, which are comparable to that of one of the current state-of-the-art TE materials, SnSe, and suggest a strong mode softening in these compounds.[62] Notably, optical phonon modes appear in low-frequency regions

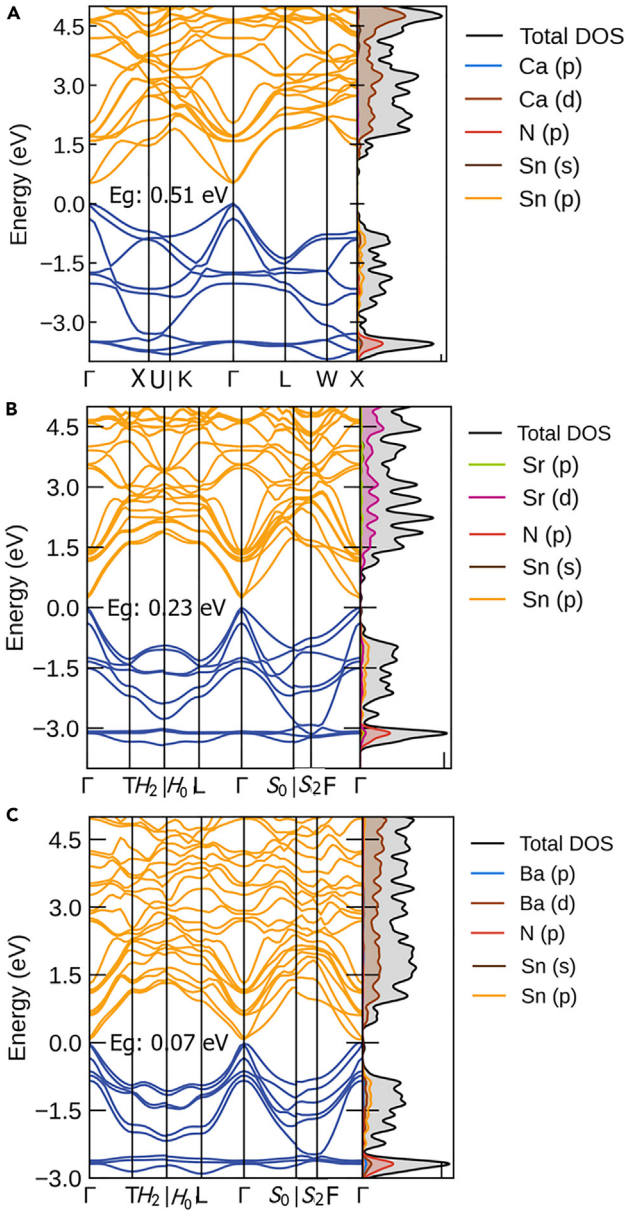

Figure 3. Band structures and projected DoS of X_6NFSn_2 calculated at the HSE06+SOC level

(A–C) Band structures and projected DoS of (A) Ca_6NFSn_2, (B) Sr_6NFSn_2, and (C) Ba_6NFSn_2 calculated at the HSE06+SOC level.

(<3 THz). Taking Ca_6NFSn_2 as an example, optical phonon with a frequency of 1.42 THz cm^{-1} at the Γ point corresponds to the [Ca_6F] and [Ca_6N] octahedra rocking motion, and the one with a frequency of 2.75 THz cm^{-1} relates to the rocking of Sn atoms. These low-frequency optical phonon modes couple with acoustic phonons. Such a coupling would be expected to increase the scattering channels for the heat-carrying acoustic phonons, which indicates potentially low LTC. Analyses of the phonon scattering rate between acoustic and optical modes are shown in part below. Similar vibrational modes are observed in Sr_6NFSn_2 and Ba_6NFSn_2 as well.

Band structure calculations (Figure 3) show that Ca_6NFSn_2 and Sr_6NFSn_2 possess direct band gaps of 0.51 and 0.23 eV at the Γ point. Unlike semiconducting

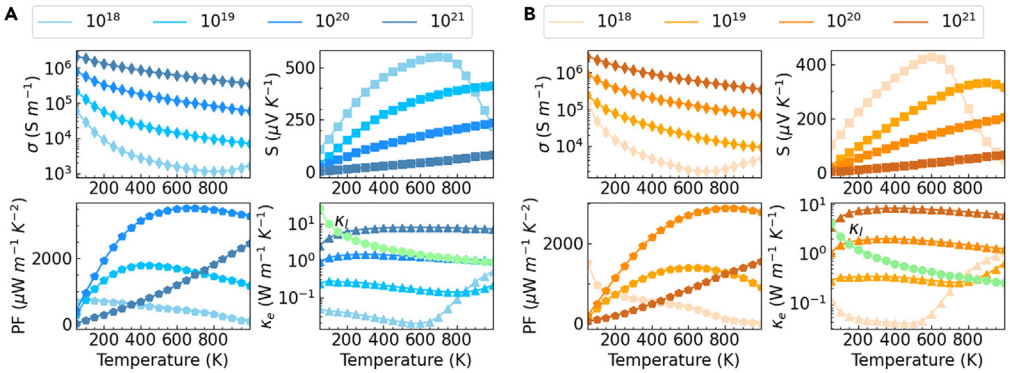

Figure 4. Calculated electrical transport properties as a function of temperature for p-type X_6NFSn_2 at four different carrier concentrations

(A and B) Calculated electrical transport properties as a function of temperature for p-type (A) Ca_6NFSn_2 and (B) Sr_6NFSn_2 at four different carrier concentrations (1.0×10^{18}–1.0×10^{21} cm^{-3}): electrical conductivity (σ), Seebeck coefficient (S), power factor (PF), and electronic thermal conductivity (κ_e). The LTC (κ_l) is displayed on the κ_e plots with green symbols for comparison.

Ca_6NFSn_2 and Sr_6NFSn_2, the band gap of Ba_6NFSn_2 almost closes, which is generally not favorable for the TE performance. The change of element X = Ca → Sr → Ba leads to the reduction of the band gaps due to the downshift of the conduction band edge mainly comprising X-atomic orbitals. One striking feature is that they all have 4- and 2-fold orbital degeneracies of the valence band edge (VBE) and the conduction band edge (CBE), respectively. The high orbital degeneracy of the VBE implies a potentially large S. Moreover, the valence band maximum (VBM) and the conduction band minimum (CBM) predominantly consist of Sn-p and nominally unoccupied X-d orbitals (see Figure 3), which suggests a cross-gap hybridization and covalent character in these compounds.[63] Owing to the cross-gap hybridization, these mixed-anion antiperovskites exhibit large valence and conduction band dispersion, indicative of small effective masses of the carriers.

Electrical transport and TE properties

The electrical transport properties of Ca_6NFSn_2 and Sr_6NFSn_2 were obtained via the momentum relaxation time approximation (MRTA) as implemented in AMSET under p-type- and n-type-doping conditions with carrier concentrations ranging from 10^{18} to 10^{21} cm^{-3}. Compared to an accurate but highly costly method like DFPT+ Wannier,[64,65] AMSET has been demonstrated to produce excellent agreement for carrier mobilities and Ss in a series of semiconductors such as Si, GaN, SnSe, Bi_2Te_3, and $CH_3NH_3PbI_3$ with experimental measurements at comparatively lower computational costs.[66] The TE performance of p-type Ca_6NFSn_2 and Sr_6NFSn_2 is discussed in detail here because these p-type compounds show higher ZTs in comparison to n-type. The corresponding data of n-type Ca_6NFSn_2 and Sr_6NFSn_2 are given in the supplemental information (Figures S2 and S3) for comparison.

Strikingly, Ca_6NFSn_2 and Sr_6NFSn_2 show good electrical transport properties. As shown in Figure 4A, the electrical conductivities of Ca_6NFSn_2 are in the range of 1.12×10^3 (at a carrier concentration of 10^{18} cm^{-3} and a temperature of 800 K) to 2.10×10^6 S m^{-1} (at a carrier concentration of 10^{21} cm^{-3} and a temperature of 50 K). At the same carrier concentrations, Sr_6NFSn_2 shows higher electrical conductivities ranging from 1.99×10^3 (700 K) to 2.64×10^6 S m^{-1} (50 K) (Figure 4B), and $CsSnI_3$ displays lower electrical conductivities from 1.03×10^2 to 5.10×10^5 S m^{-1} (Figure S4). When calculating the hole mobilities, three scattering processes, namely the acoustic deformation potential (ADP), ionized impurity (IMP), and polar-optical phonon (POP) scattering, were considered. As shown in Figure S5, the

POP scattering process dominantly limits the hole mobility in Ca_6NFSn_2 and Sr_6NFSn_2 at RT and higher temperatures. Notably, the p-type electrical conductivities of Ca_6NFSn_2 and Sr_6NFSn_2 are at least an order of magnitude higher than those of $CsSnI_3$ at fixed carrier concentrations of 10^{18} and 10^{19} cm^{-3}. As the carrier concentrations are further increased to 10^{20} and 10^{21} cm^{-3}, the electrical conductivities of the two mixed-anion antiperovskites increase by 4-fold compared to those of $CsSnI_3$ at the same carrier concentrations. It has been experimentally pointed out that the low σ of $CsSnI_3$ restricts the TE performance despite its extremely low LTC; correspondingly, the obtained maximum *ZT* values of $CsSnI_3$ are 0.08 at RT and 0.175 at 550 K.[10,34,35] Heavy hole (electron) doping to improve the electrical conductivities is thus crucial to boost the potential of $CsSnI_3$ as a promising TE material. We note that the calculated electrical conductivities of Ca_6NFSn_2 and Sr_6NFSn_2 are on a par with that of the current flagship chalcogenide TE material SnSe at the doping level of 10^{19} cm^{-3} using similar levels of theory.[67] We focus our discussion on this order of magnitude because the optimum *ZT*s of single-crystal and polycrystalline SnSe are obtained at this level and, on the other hand, the *ZT* maxima for Ca_6NFSn_2 and Sr_6NFSn_2 appear for carrier concentrations in the region of 10^{19} cm^{-3}.[15,68] The dopability of Ca_6NFSn_2 will be evaluated in future work. However, as we noticed, the dominant native defects (vacancies) in ternary nitride antiperovskites show low formation energies and efficient p-type or n-type self-doping.[69,70]

In addition to high electrical conductivities, Ca_6NFSn_2 and Sr_6NFSn_2 have decent *S*s. Their *S*s are on a par with that of SnSe and 1.6-fold higher than that of $CsSnI_3$ at the doping level of 10^{19} cm^{-3}. At the carrier concentration of 10^{18} cm^{-3}, *S*s of Ca_6NFSn_2 (Sr_6NFSn_2) increase smoothly to a peak at around 700 K (600 K) and then start to decline, as seen in Figure 4. The observed saturation of *S*s at 10^{18} cm^{-3} at high temperatures can be attributed to the bipolar effect, which occurs in small-band-gap materials, especially at high temperature.[71–73] When the carrier concentration is elevated to 10^{19} cm^{-3}, the saturation of *S*s is relieved, to some extent, and the peaks of *S*s shift to higher temperatures, namely 1,000 and 950 K for Ca_6NFSn_2 and Sr_6NFSn_2, respectively. At even higher hole-doping levels (10^{20} and 10^{21} cm^{-3}), the *S*s increase monotonically as the temperature rises. The combination of high electrical conductivities and decent *S*s of Ca_6NFSn_2 and Sr_6NFSn_2 leads to their p-type power factors (PFs) spanning the ranges of 40–3,470 and 5–2,886 $\mu W\ m^{-1}\ K^{-2}$, respectively. For Ca_6NFSn_2 (Sr_6NFSn_2), the PF computed at a fixed carrier concentration of 10^{21} cm^{-3} increases as the temperature rises, while those PFs calculated at the other three carrier concentrations (from 10^{18} to 10^{20} cm^{-3}) peak at 100 (50 K), 400 (600 K), and 600 K (900 K), as shown in Figure 4.

The κ is composed of κ_e and κ_l. κ_l is often the limiting factor for the TE performance of promising candidates.[4] The calculated κ_l of Ca_6NFSn_2 at RT is 2.94 $W\ m^{-1}\ K^{-1}$, and it further decreases to 0.88 $W\ m^{-1}\ K^{-1}$ at 1,000 K (Figure 4). Sr_6NFSn_2 show lower calculated κ_ls, viz. 0.83 and 0.25 $W\ m^{-1}\ K^{-1}$ at RT and 1,000 K, respectively. The RT κ_ls of Ca_6NFSn_2 and Sr_6NFSn_2 are comparable to the calculated κ_ls of PbS (2.19 $W\ m^{-1}\ K^{-1}$) and SnSe (0.52 $W\ m^{-1}\ K^{-1}$).[62,67,74] Notably, the ultralow LTC ($\kappa_l < 1$ $W\ m^{-1}\ K^{-1}$) of Ca_6NFSn_2 and Sr_6NFSn_2 at high temperatures is a feature of high-efficiency TEs. More discussion about the origin of the low κ_l is given in the following section. Our calculations of κ_l are based on the relaxation-time approximation (RTA), which accounts for three-phonon scattering mechanisms and neglects other scattering processes like electron-phonon and phonon-defect scattering.[75] The RTA also does not consider the collective phonon excitations that appear in a full solution of the linearized Boltzmann transport equation (LBTE)[76] and thus tends to possibly underestimate κ_l.[77,78] However, the omission of collective phonon

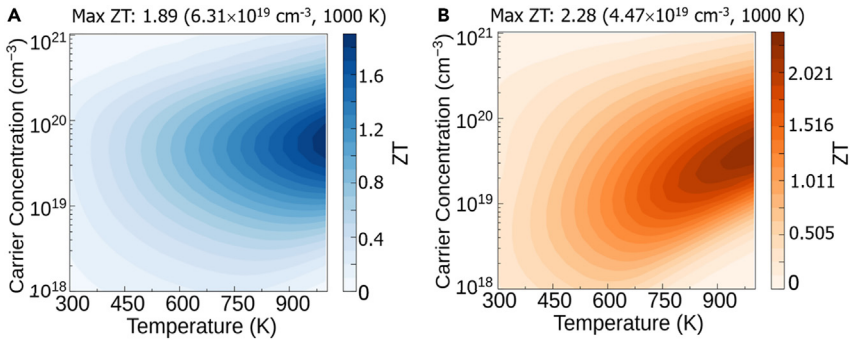

Figure 5. Predicted thermoelectric figures of merit (*ZT*) of p-type X_6NFSn_2 as a function of temperature and carrier concentration

(A) Ca_6NFSn_2.

(B) Sr_6NFSn_2.

excitations partially compensates for the neglect of other scattering mechanisms, which often are in good agreement with experiments.[26,79] In light of the lower LTC of Ca_6NFSn_2 and Sr_6NFSn_2, point defect scattering and nanostructuring (e.g., grain boundary effect) are not taken into consideration, as they may be not effective at reducing the LTC further, i.e., the mean-free path is already short, at less than 10 nm (see the following section).

Despite the low κ_l, attention should be paid to the other component of the κ, κ_e, as high σ results in high κ_e. As shown in Figure 4, when $n_p \leq 10^{20}$ cm^{-3}, the κ_e of Ca_6NFSn_2 is smaller than its κ_l, and the latter thus dominates the thermal transport, which means that thermal losses through phonons would be more paramount for TE performance. When the carrier concentration exceeds 10^{20} cm^{-3}, the electronic contribution becomes predominant above 210 K. For Sr_6NFSn_2, κ_e is smaller than κ_l when $n_p \leq 10^{19}$ cm^{-3} and T <810 K. At a high carrier concentration of 10^{20} cm^{-3}, κ_e dominates above 190 K. When the carrier concentration further increases to 10^{21} cm^{-3}, κ_e is larger than κ_l above 76 K, and thermal losses by charge carriers are dominant.

We combine the calculated electrical transport properties and κs to predict the TE *ZT*s for Ca_6NFSn_2 and Sr_6NFSn_2 as a function of carrier concentration and temperature (Figure 5). A maximum average *ZT* of 1.89 for p-type Ca_6NFSn_2 is predicted at a carrier concentration of 6.31×10^{19} cm^{-3} and T = 1,000 K, and the maximum of the average *ZT* of p-type Sr_6NFSn_2 (2.28) is obtained for a carrier concentration at 4.47×10^{19} cm^{-3} and T = 1,000 K. *ZT* values of Ca_6NFSn_2 are isotropic, while those of Sr_6NFSn_2 are anisotropic. *ZT*s of Sr_6NFSn_2 are 2.25 and 2.34 along the a/b and c directions, respectively, which are close. These optimum hole carrier concentration and temperature values balance the electrical and thermal properties of two materials, which could be achieved experimentally based on a series of compounds with similar-composition Ca_2NI and Ba_2NX (X = F, Cl, Br) samples that are prepared at high temperature (~1,000 K); Zn_2NX (X = Cl, Br) are synthesized at ~850 K and are thermally stable up to 1,023 K.[59–61] Moreover, the dominant competing phases of Ca_6NFSn_2 and Sr_6NFSn_2 are also stable at ~1,000 K.[80] Thus, the thermal stability of targeted compounds up to 1,000 K seems to be possible. The optimal hole-doping concentration (~10^{19} cm^{-3}) could be obtained via self-doping.[69,70] These *ZT* values are the highest accessible so far for p-type perovskite-related TE materials at middle-high temperature,[10,14,26,27,37] while they are lower than the *ZT* of SnSe (2.81) computed at a similar level of theory.[67] *ZT* values of 3.1 and 2.0 have been

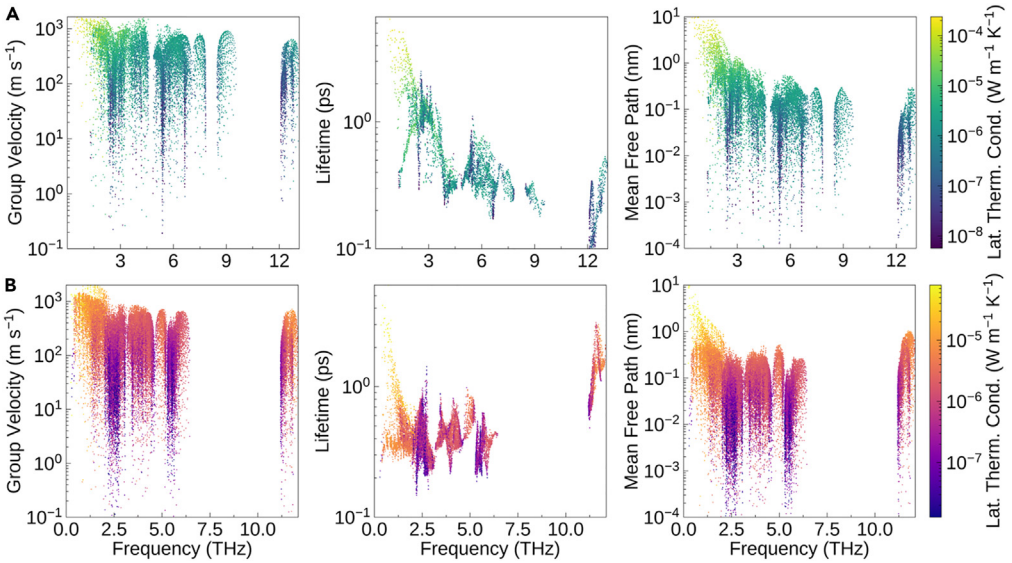

Figure 6. Analysis of the isotropically averaged modal group velocity, lifetimes, and mean-free paths of X_6NFSn_2

(A and B) Analysis of the isotropically averaged modal group velocity, lifetimes, and mean-free paths of X_6NFSn_2 (A) and Sr_6NFSn_2 (B) at 1,000 K, respectively. This analysis was performed using ThermoParser.[100] The data points are color-coded by the modal contributions to κ_l. κ_l value ranges are coded from blue to yellow and purple to yellow (low to high κ_l) for Ca_6NFSn_2 and Sr_6NFSn_2, respectively.

experimentally reported for polycrystalline and single-crystal SnSe at 783 and 773 K, respectively.[15,68] The above results suggest that Ca_6NFSn_2 and Sr_6NFSn_2 are potentially promising p-type perovskite TE materials.

Origin of low LTC

FC expansions (up to the third order) were obtained by a combination of machine learning and first-principles calculations. Based on the FCs, κ_l was computed within single-mode RTA (SM-RTA) as a sum of contributions from individual phonon modes λ following

$$\kappa_l = \frac{1}{NV}\sum C_\lambda \nu_\lambda \otimes \nu_\lambda \tau_\lambda \qquad \text{(Equation 1)}$$

where N is the number of wavevectors used for the Brillouin zone (BZ) integration and V is the volume of the unit cell. C_λ, ν_λ, and τ_λ are the modal heat capacities, the group velocities, and phonon lifetimes, respectively. Scatterplots of the three quantities against the phonon frequency can be used to evaluate the contributions of the individual modes to κ_l. The influence of C_λ on κ_l is not accounted for here as it is a shallow function of the phonon frequency, and the variation between phonon modes is thus minimal.

The group velocities of Ca_6NFSn_2 and Sr_6NFSn_2 are within the range of 10^{-1} to 10^3 m s^{-1} (left columns of Figure 6). The fastest modes (~1,000 m s^{-1}) are seen around 1–3 THz due to the dispersive phonon bands at these frequencies. The phonon lifetimes in Ca_6NFSn_2 and Sr_6NFSn_2 at 1,000 K and RT vary from 0.1 to 5 and 0.1 to 3 ps, respectively, as shown in the middle columns of the Figures 6 and S6. The modes with the longest modal phonon lifetimes (<4 ps) mainly appear in the low-frequency ranges (<3 THz). Notably, at 1,000 K, there is a group of modes below 3 THz in Ca_6NFSn_2 and Sr_6NFSn_2, of which the phonon lifetimes are shorter than 1 ps, indicative of strong phonon scattering and possibly large anharmonicity.[81] The 1,000 K phonon lifetimes of the mid-frequency modes (3.5–9 THz for Ca_6NFSn_2 and 3–6.5

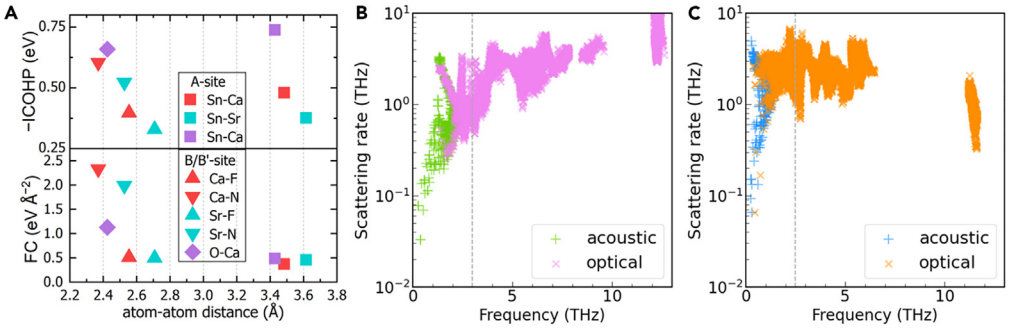

Figure 7. Analysis of the interatomic chemical bond strength

(A) Integrated crystal orbital Hamilton population (−ICOHP) (top) and force constants (FCs) (bottom) between anions centered at the A site and the B/B′ site and cations at the X site.

(B) Mode-resolved scattering rates at 1,000 K for Ca_6NFSn_2 as a function of the phonon frequency.

(C) Mode-resolved scattering rates at 1,000 K for Sr_6NFSn_2 as a function of the phonon frequency.

THz for Sr_6NFSn_2) are all below 1 ps, and high-frequency N-based modes have shorter lifetimes in Ca_6NFSn_2 than in Sr_6NFSn_2. The phonon lifetime spectra at RT show a similar spread but longer lifetimes with respect to those at 1,000 K (see Figure S6). Strikingly, the overall RT spectra of ν_λ and τ_λ calculated from third-order perturbation theory are comparable to those of the hybrid perovskite $CH_3NH_3PbI_3$, for which an ultralow LTC (0.086 W m^{-1} K^{-1}) has been predicted.[82] The combination of overall short modal lifetimes and low group velocities results in a relatively short modal mean-free path (<10 nm at 1,000 K and <100 nm at RT) (Figure 6 and S6) and thus leads to low averaged κs of 2.94 (0.88 W m^{-1} K^{-1}) and 0.83 W m^{-1} K^{-1} (0.25 W m^{-1} K^{-1}) at RT (T = 1,000 K) for Ca_6NFSn_2 and Sr_6NFSn_2, respectively.

Besides the modal analysis, chemical bond characteristics, viz. chemical bonding strength and bond anharmonicity, of Ca_6NFSn_2 and Sr_6NFSn_2 are discussed. The interatomic bond strength of these new materials is evaluated based on the FCs and integrated crystal orbital Hamilton population (ICOHP) analyses, which imply the bond strength.[83] As a representative known antiperovskite, Ca_3OSn is taken into account as well. The bond strength generally decreases as the atom-atom distance increases. As shown in Figure 7A, Sn−X and X−N (X = Ca/Sr) bonds follow the trend, and their −ICOHPs are small with respect to SnSe,[84] indicative of the weak bond strength. However, X−F (X = Ca/Sr) bonds disobey the trend and exhibit the smallest −ICOHP among all bonds. In addition to the small −ICOHP, the FCs of F−X (X = Ca/Sr) are rather small. The FCs of X−Sn (X = Ca/Sr) are the smallest among all bonds, suggesting the role of Sn atoms acting as cage rattlers. Meanwhile, the O−Ca bonds are stiffer than X−N (X = Ca/Sr) bonds, which is consistent with the trend of LTC, i.e., the calculated LTC of Ca_3OSn (1.73 W m^{-1} K^{-1} at 1,000 K) is larger than those of Ca_6NFSn_2 and Sr_6NFSn_2 (0.83 and 0.25 W m^{-1} K^{-1} at 1,000 K). The combined analysis of −ICOHPs and FCs unravels the weak interatomic bond strength and soft lattice of Ca_6NFSn_2 and Sr_6NFSn_2. The soft lattice would impede phonon propagation and result in low LTC. Moreover, weak interatomic bond strength would introduce low-frequency vibrations, referred to as soft low-frequency optical phonons, which are indeed observed in Ca_6NFSn_2 and Sr_6NFSn_2 (Figure 2). These low-frequency optical modes do couple with acoustic phonons and contribute to the scattering rate, as shown in Figures 7B and 7C. The scattering rates of most phonon modes are within the range from 0.1 to 1 THz, which are comparable to those of SnSe and $CH_3NH_3PbI_3$.[82,85] The optical and acoustic phonon resonant effect increases the scattering rate in low-frequency regions and scattering channels

for the heat-carrying acoustic phonons, which is supported by Sr_6NFSn_2 possessing a larger scattering rate but a lower κ_l than Ca_6NFSn_2 (see Figures 7B and 7C). Additionally, as displayed in Figure S7 (cumulative LTC vs. frequency), the low-frequency modes (<3 THz), which are dominated by acoustic and optical modes, contribute to at least 65% of the LTC, further corroborating the phonon resonant scattering mechanism in these new double antiperovskites.

In addition to the weak chemical bond strength, lattice vibrational anharmonicity is another factor influencing the κ_l, as anharmonicity of the chemical bonds drives the phonon–phonon Umklapp and normal processes limiting the LTC.[86] Here, the mode Grüneisen parameter (γ) and the average Grüneisen parameter are employed to evaluate the bond anharmonicity. As displayed in Figure S8, the mode Grüneisen parameters of Ca_6NFSn_2 are positive. In contrast, the mode Grüneisen parameters of Sr_6NFSn_2 can be negative. The average RT Grüneisen parameters obtained based on the method given in Shao et al.[87] for Ca_6NFSn_2, Sr_6NFSn_2, and Ca_3OSn are 1.65, 1.37, and 1.54, respectively. The average Grüneisen parameters of Ca_6NFSn_2, Sr_6NFSn_2, and Ca_3OSn are on a par with some state-of-the-art TE materials such as PbTe (1.49).[13] Compared to Ca_6NFSn_2, Sr_6NFSn_2 exhibits a lower κ_l within the whole range of temperatures (Figure 4), and it possesses a smaller average Grüneisen parameter. Additionally, Sr has a larger atomic radius than Ca, which makes its valence shell and the electron clouds surrounding the Sr atoms larger than those of Ca. As seen in Figure S9, electrons are indeed more localized around Sr than Ca (higher electron localization function [ELF] for Sr), which possibly leads to a stronger lattice vibrational energy. Overall, the weak chemical bonding and strong bond anharmonicity are the macroscopic factors of the low κ_l in Ca_6NFSn_2 and Sr_6NFSn_2. Meanwhile phonon resonant scattering and Umklapp scattering are the dominant mechanisms affecting their κ.

Conclusion

In summary, we have discovered new multi-anion antiperovskites X_6NFSn_2 (X = Ca, Sr, and Ba) via anion mutation and global structure searches. Their phase stabilities were identified by first-principles calculations. Notably, Ca_6NFSn_2 and Sr_6NFSn_2 show superior electrical conductivities combined with low LTC at RT (<3 W m^{-1} K^{-1}) and high temperature (<1 W m^{-1} K^{-1}). The weak chemical bonding between the heavy-atom cage-rattler Sn and alkaline-earth metal (Ca and Sr) inducing low-frequency optical modes coupling with heat-carrying acoustic phonons in combination with strong bond anharmonicity results in the predicted low LTC in Ca_6NFSn_2 and Sr_6NFSn_2. Owing to the high electrical conductivities and effective thermal insulation, the maximum ZT values of p-type Ca_6NFSn_2 and Sr_6NFSn_2 are predicted to be 1.89 and 2.28 at 1,000 K, respectively, which are currently higher than the reported perovskite oxides and halides. Our work of exploring multi-anion antiperovskites X_6NFSn_2 (X = Ca, Sr, and Ba) realizes the PGEC concept for promising TE materials within the vast family of perovskite structures.

EXPERIMENTAL PROCEDURES

Resource availability

Lead contact

Further information and requests for resources should be directed to and will be fulfilled by the lead contact, Dan Han (d.han@bham.ac.uk).

Materials availability

The materials in this study will be made available upon reasonable request.

Data and code availability

All data reported in this paper will be shared by the lead contact upon request. This paper does not report original code.

Computational methods

For the crystal structure predictions of X_6NFSn_2 (X = Ca, Sr, and Ba), AIRSS and particle swarm optimization were utilized. AIRSS is powerful and highly parallel for locating low-energy structures with a given composition.[49,50] The search of each composition (Ca_6NFSn_2, Sr_6NFSn_2, Ba_6NFSn_2) was constrained with the number of atoms in the reduced formula of 10. A comparative search including two reduced formula units (20 atoms) was performed for Ca_6NFSn_2, and it finds the same low-energy structures as the search with one reduced formula. For each composition, over 2,000 random structures were generated and relaxed. The plane wave density functional theory code CASTEP with core-corrected ultrasoft pseudopotentials generated as defined in the built-in QC5 library was used for the searching.[88] A plane-wave cutoff energy was set to 350 eV. The reciprocal space sampling was performed by using Monkhorst-Pack grids with a spacing of 0.07 × 2π $Å^{-1}$. CALYPSO was utilized for the crystal structure prediction of X_6NFSn_2 (X = Ca, Sr, and Ba) as well.[51,52] Thirty generations of structures with a population of 30 were considered. The local optimization calculations were performed three times for each structure generated by CALYPSO with a gradually increasing force convergence criteria. All the low-energy structures of X_6NFSn_2 were found around the 20^{th} generation, hence establishing the validity of this crystal structure search strategy.

Afterward, for further relaxations and property calculations of the low-energy structures generated by AIRSS, the Vienna Ab initio Simulation Package (VASP) was used.[89] For these calculations, a plane-wave cutoff energy of 520 eV, Γ-centered Monkhorst-Pack grids with a grid spacing of 0.03 × 2π $Å^{-1}$, and the projector-augmented wave applying the parameterization of the exchange-correction potential given by Perdew-Burke-Ernzerhof (PBE) were used.[90] The convergence criteria for the energy and force were set to 10^{-5} eV and 0.01 eV/Å, respectively. The Heyd-Scuseria-Ernzerhof functional with 25% nonlocal Hartree-Fock exchange (HSE06) was employed for the electronic structure calculations.[91] The spin-orbit coupling (SOC) effect was included. The postprocessing of electronic structure was carried out by sumo.[92] Calculations of harmonic lattice dynamics (phonon spectrum and atom-projected phonon density of states) were calculated based on the frozen phonon method implemented in the Phonopy package.[93] 80-atom, 270-atom, and 270-atom supercells were used for phonon calculations of Ca_6NFSn_2, Sr_6NFSn_2, and Ba_6NFSn_2, respectively. The harmonic phonon spectrum of a larger supercell with 320 atoms of Ca_6NFSn_2 was calculated for testing the convergency, which shows that the phonon dispersions are reasonably converged with a small 80-atom supercell created from the primitive cell (Figure S10).

The electrical transport properties were calculated using the AMSET software package.[66] The code uses MRTA to calculate the scattering rates and carrier mobilities.[94] Here, three scattering processes, namely ADP, IMP, and POP scattering, were considered. The material parameters including high-frequency and static dielectric constants, elastic constants, polar optical phonon frequency, and deformation potentials required as input by this method were all obtained using first-principles calculations. To get the deformation potentials, calculations were performed using HSE06 functional. The high-frequency dielectric constants, static dielectric constants, and "effective polar optical phonon frequency" were obtained using density-functional perturbation theory (DFPT) with HSE06 functional.[95] The SOC effect

was not considered for deformation potential, as it is reported that the SOC effect has a negligible effect on this property of ABX_3 (A = K, Rb, Cs; B = Ge, Sn, Pb; X = Cl, Br, I) halide perovskites.[96] Elastic constants were calculated through the stress-strain approach with the PBE exchange-correlation functional. The transport properties need to be converged with respect to an interpolation factor, which controls the number of k-points in the interpolated band structures. Convergence testing results of Ca_6NFSn_2 are provided in Table S5. Dense Fourier interpolated meshes of 69 × 69 × 69 and 37 × 37 × 37 were chosen (the original input k-point meshes of the electronic band structures computed using DFT were 12 × 12 × 12 and 8 × 8 × 8) for Ca_6NFSn_2 and Sr_6NFSn_2 by balancing the computational cost and accuracy. Structures optimized with tight convergence criteria for energy (10^{-8} eV) and force (0.001 eV/Å) and the same tight setting were used for the calculations of harmonic phonon properties and electrical transport properties. Specific material parameters used to compute electrical transport properties are given in Table S6.

The κ_l was calculated by solving the phonon BTE under the SM-RTA.[75,97] Phonon linewidths (inverse phonon lifetimes) were computed perturbatively to the third order by considering three-phonon scattering processes.[75] FCs (up to the third order) were obtained via the combination of machine learning (via the HIPHIVE package) and first-principles calculations. The utility of this approach was demonstrated via several examples like SnSe and monolayers of MoS_2.[98,99] For Ca_6NFSn_2, 20 320-atom supercells with random displacements of standard deviation of 0.02 Å were generated. The PBE functional and the Γ point were used for calculating FCs. The cutoff radii for the two-, three-, and four-body clusters were 8, 5, and 4 Å, respectively. The linear least-squares method was used for fitting with a train-test ratio of 9:1. Similar settings were used for Sr_6NFSn_2, while larger supercells (360 atoms) were employed, and the DFT calculations were performed using the HSE06 functional. In both cases, the R^2 scores were higher than 0.99, indicating a high quality for the fittings. In addition, the phonon dispersion spectrum computed from the fitted (second-order) FCs matches well with that from standalone Phonopy calculations, as shown in Figure S11A. The LTCs calculated from the FCs that were obtained via HIPHIVE also agree well with those directly computed from the FCs obtained by Phono3py (see Figure S11B). The LTCs of Ca_6NFSn_2 were converged with respect to the q-point sampling density (Figure S11C), leading to 18 × 18 × 18 and 15 × 15 × 15 meshes for Ca_6NFSn_2 and Sr_6NFSn_2 being chosen, respectively. ZT was obtained by using ThermoParser, the validation of which has been examined by literature.[100–102]

SUPPLEMENTAL INFORMATION

Supplemental information can be found online at https://doi.org/10.1016/j.matt.2023.10.022.

ACKNOWLEDGMENTS

D.H., H.E., S.S.R., W.S., and T.B. acknowledge support from Deutsche Forschungsgemeinschaft (DFG, German Research Foundation) under Germany's Excellence Strategy (Excellence Cluster e-conversion–EXC 2089/1–390776260). K.B.S. and D.O.S. acknowledge support from the European Research Council (grant 758345). D.H. and H.E. gratefully acknowledge the Gauss Centre for Supercomputing e.V. (https://www.gauss-centre.eu) for funding this project by providing computing time on the GCS Supercomputer SuperMUC-NG at the Leibniz Supercomputing Centre (https://www.lrz.de). B.Z. acknowledges the use of the UCL Myriad High

Performance Computing Facility (Myriad@UCL) and the ARCHER2 UK National Supercomputing Service (http://www.archer2.ac.uk), which is supported by the HEC Materials Chemistry Consortium funded by EPSRC (EP/R029431). D.H. and D.O.S. acknowledge the use of the University of Birmingham BlueBEAR HPC service, which provides a High Performance Computing service to the University's research community. See http://www.birmingham.ac.uk/bear for more details.

AUTHOR CONTRIBUTIONS

D.H. conceived the idea and wrote the draft. D.H. and B.Z. conducted the theoretical simulations and analyzed the data. Z.C. performed the crystal structure prediction by CALYPSO. K.B.S. provided software resources and assisted in the analysis of TE properties. S.S.R., W.S., and T.B. carried out validation and provided resources for the project. D.O.S. provided conceptualization and software resources. H.E. provided funding acquisition and project administration. All authors contributed to writing, review, and editing.

DECLARATION OF INTERESTS

The authors declare no competing interests.

Received: May 22, 2023
Revised: September 10, 2023
Accepted: October 18, 2023
Published: November 15, 2023

REFERENCES

1. Nolas, G.S., Sharp, J., and Goldsmid, J. (2001). Thermoelectrics: Basic Principles and New Materials Developments*45* (Springer Science & Business Media).

2. Finn, P.A., Asker, C., Wan, K., Bilotti, E., Fenwick, O., and Nielsen, C.B. (2021). Thermoelectric Materials: Current Status and Future Challenges. Front. Electron. Mater. *1*, 677845. https://doi.org/10.3389/femat.2021.677845.

3. Ioffe, A.F., Stil'bans, L.S., Iordanishvili, E.K., Stavitskaya, T.S., Gelbtuch, A., and Vineyard, G. (1959). Semiconductor thermoelements and thermoelectric cooling. Phys. Today *12*, 42. https://doi.org/10.1063/1.3060810.

4. Beekman, M., Morelli, D.T., and Nolas, G.S. (2015). Better thermoelectrics through glass-like crystals. Nat. Mater. *14*, 1182–1185. https://doi.org/10.1038/nmat4461.

5. Snyder, G.J., and Toberer, E.S. (2008). Complex thermoelectric materials. Nat. Mater. *7*, 105–114.

6. Slack, G.A. (1995). CRC Handbook of Thermoelectrics (CRC press).

7. Morelli, D.T., and Meisner, G.P. (1995). Low temperature properties of the filled skutterudite $CeFe_4Sb_{12}$. J. Appl. Phys. *77*, 3777–3781. https://doi.org/10.1063/1.358552.

8. Sales, B., Mandrus, D., and Williams, R.K. (1996). Filled skutterudite antimonides: a new class of thermoelectric materials. Science *272*, 1325–1328. https://doi.org/10.1126/science.272.5266.1325.

9. Cohn, J.L., Nolas, G.S., Fessatidis, V., Metcalf, T.H., and Slack, G.A. (1999). Glasslike heat conduction in high-mobility crystalline semiconductors. Phys. Rev. Lett. *82*, 779–782. https://doi.org/10.1103/PhysRevLett.82.779.

10. Xie, H., Hao, S., Bao, J., Slade, T.J., Snyder, G.J., Wolverton, C., and Kanatzidis, M.G. (2020). All-inorganic halide perovskites as potential thermoelectric materials: dynamic cation off-centering induces ultralow thermal conductivity. J. Am. Chem. Soc. *142*, 9553–9563. https://doi.org/10.1021/jacs.0c03427.

11. Wu, T., and Gao, P. (2018). Development of perovskite-type materials for thermoelectric application. Materials *11*, 999. https://doi.org/10.3390/ma11060999.

12. Feng, L., Shiga, T., and Shiomi, J. (2015). Phonon transport in perovskite $SrTiO_3$ from first principles. APEX *8*. 071501. https://doi.org/10.7567/apex.8.071501.

13. Xiao, Y., Chang, C., Pei, Y., Wu, D., Peng, K., Zhou, X., Gong, S., He, J., Zhang, Y., Zeng, Z., and Zhao, L.D. (2016). Origin of low thermal conductivity in SnSe. Phys. Rev. B *94*, 125203. https://doi.org/10.1103/PhysRevB.94.125203.

14. Shi, X.-L., Wu, H., Liu, Q., Zhou, W., Lu, S., Shao, Z., Dargusch, M., and Chen, Z.-G. (2020). $SrTiO_3$-based thermoelectrics: Progress and challenges. Nano Energy *78*, 105195. https://doi.org/10.1016/j.nanoen.2020.105195.

15. Zhou, C., Lee, Y.K., Yu, Y., Byun, S., Luo, Z.-Z., Lee, H., Ge, B., Lee, Y.-L., Chen, X., Lee, J.Y., et al. (2021). Polycrystalline SnSe with a thermoelectric figure of merit greater than the single crystal. Nat. Mater. *20*, 1378–1384. https://doi.org/10.1038/s41563-021-01064-6.

16. Tan, G., Shi, F., Hao, S., Zhao, L.-D., Chi, H., Zhang, X., Uher, C., Wolverton, C., Dravid, V.P., and Kanatzidis, M.G. (2016). Non-equilibrium processing leads to record high thermoelectric figure of merit in PbTe–SrTe. Nat. Commun. *7*, 12167–12169. https://doi.org/10.1038/ncomms12167.

17. Ren, G.-K., Wang, S., Zhou, Z., Li, X., Yang, J., Zhang, W., Lin, Y.-H., Yang, J., and Nan, C.-W. (2019). Complex electronic structure and compositing effect in high performance thermoelectric BiCuSeO. Nat. Commun. *10*, 2814. https://doi.org/10.1038/s41467-019-10476-7.

18. Quinn, R.J., and Bos, J.-W.G. (2021). Advances in half-Heusler alloys for thermoelectric power generation. Mater. Adv. *2*, 6246–6266. https://doi.org/10.1039/D1MA00707F.

19. Stranks, S.D., Eperon, G.E., Grancini, G., Menelaou, C., Alcocer, M.J.P., Leijtens, T., Herz, L.M., Petrozza, A., and Snaith, H.J. (2013). Electron-hole diffusion lengths exceeding 1 micrometer in an organometal trihalide perovskite absorber. Science *342*, 341–344. https://doi.org/10.1126/science.1243982.

20. Shi, D., Adinolfi, V., Comin, R., Yuan, M., Alarousu, E., Buin, A., Chen, Y., Hoogland, S., Rothenberger, A., Katsiev, K., et al. (2015). Low trap-state density and long carrier diffusion in organolead trihalide perovskite single crystals. Science *347*, 519–522. https://doi.org/10.1126/science.aaa2725.

21. Yoo, J.J., Seo, G., Chua, M.R., Park, T.G., Lu, Y., Rotermund, F., Kim, Y.-K., Moon, C.S., Jeon, N.J., Correa-Baena, J.-P., et al. (2021). Efficient perovskite solar cells via improved carrier management. Nature *590*, 587–593. https://doi.org/10.1038/s41586-021-03285-w.

22. Hu, X., Zhang, X., Liang, L., Bao, J., Li, S., Yang, W., and Xie, Y. (2014). High-performance flexible broadband photodetector based on organolead halide perovskite. Adv. Funct. Mater. *24*, 7373–7380. https://doi.org/10.1002/adfm.201402020.

23. Guo, R., Han, D., Chen, W., Dai, L., Ji, K., Xiong, Q., Li, S., Reb, L.K., Scheel, M.A., Pratap, S., et al. (2021). Degradation mechanisms of perovskite solar cells under vacuum and one atmosphere of nitrogen. Nat. Energy *6*, 977–986. https://doi.org/10.1038/s41560-021-00912-8.

24. Stoumpos, C.C., Malliakas, C.D., and Kanatzidis, M.G. (2013). Semiconducting tin and lead iodide perovskites with organic cations: phase transitions, high mobilities, and near-infrared photoluminescent properties. Inorg. Chem. *52*, 9019–9038. https://doi.org/10.1021/ic401215x.

25. Pisoni, A., Jaćimović, J., Barišić, O.S., Spina, M., Gaál, R., Forró, L., and Horváth, E. (2014). Ultra-low thermal conductivity in organic–inorganic hybrid perovskite $CH_3NH_3PbI_3$. J. Phys. Chem. Lett. *5*, 2488–2492. https://doi.org/10.1021/jz5012109.

26. Lee, W., Li, H., Wong, A.B., Zhang, D., Lai, M., Yu, Y., Kong, Q., Lin, E., Urban, J.J., Grossman, J.C., and Yang, P. (2017). Ultralow thermal conductivity in all-inorganic halide perovskites. Proc. Natl. Acad. Sci. USA *114*, 8693–8697. https://doi.org/10.1073/pnas.171174411.

27. Haque, M.A., Kee, S., Villalva, D.R., Ong, W.L., and Baran, D. (2020). Halide perovskites: thermal transport and prospects for thermoelectricity. Adv. Sci. *7*, 1903389. https://doi.org/10.1002/advs.201903389.

28. Zhou, Y., Wang, J., Luo, D., Hu, D., Min, Y., and Xue, Q. (2022). Recent progress of halide perovskites for thermoelectric application. Nano Energy *94*, 106949. https://doi.org/10.1016/j.nanoen.2022.106949.

29. Yin, W.J., Shi, T., and Yan, Y. (2014). Unusual defect physics in $CH_3NH_3PbI_3$ perovskite solar cell absorber. Appl. Phys. Lett. *104*. 063903. https://doi.org/10.1063/1.4864778.

30. Walsh, A., Scanlon, D.O., Chen, S., Gong, X.G., and Wei, S.H. (2015). Self-regulation mechanism for charged point defects in hybrid halide perovskites. Angew. Chem. *127*, 1811–1814. https://doi.org/10.1002/ange.201409740.

31. Du, M.-H. (2015). Density Functional Calculations of Native Defects in $CH_3NH_3PbI_3$: Effects of Spin-Orbit Coupling and Self-Interaction Error. J. Phys. Chem. Lett. *6*, 1461–1466. https://doi.org/10.1021/acs.jpclett.5b00199.

32. Chung, I., Song, J.-H., Im, J., Androulakis, J., Malliakas, C.D., Li, H., Freeman, A.J., Kenney, J.T., and Kanatzidis, M.G. (2012). $CsSnI_3$: semiconductor or metal? High electrical conductivity and strong near-infrared photoluminescence from a single material. High hole mobility and phase-transitions. J. Am. Chem. Soc. *134*, 8579–8587. https://doi.org/10.1021/ja301539s.

33. Takahashi, Y., Hasegawa, H., Takahashi, Y., and Inabe, T. (2013). Hall mobility in tin iodide perovskite $CH_3NH_3SnI_3$: Evidence for a doped semiconductor. J. Solid State Chem. *205*, 39–43. https://doi.org/10.1016/j.jssc.2013.07.008.

34. Tang, W., Liu, T., and Fenwick, O. (2022). High thermoelectric performance based on $CsSnI_3$ thin films with improved stability. J. Mater. Chem. A *10*, 7020–7028. https://doi.org/10.1039/D1TA11093D.

35. Zheng, L., Nozariasbmarz, A., Hou, Y., Yoon, J., Li, W., Zhang, Y., Wu, H., Yang, D., Ye, T., Sanghadasa, M., et al. (2022). A universal all-solid synthesis for high throughput production of halide perovskite. Nat. Commun. *13*, 7399. https://doi.org/10.1038/s41467-022-35122-7.

36. Haque, E., and Hossain, M.A. (2019). DFT based study on structural stability and transport properties of Sr_3AsN: A potential thermoelectric material. J. Mater. Res. *34*, 2635–2642. https://doi.org/10.1557/jmr.2019.146.

37. Ochi, M., and Kuroki, K. (2019). Comparative first-principles study of antiperovskite oxides and nitrides as thermoelectric material: multiple Dirac cones, low-dimensional band dispersion, and high valley degeneracy. Phys. Rev. Appl. *12*. 034009. https://doi.org/10.1103/PhysRevApplied.12.034009.

38. Okamoto, Y., Sakamaki, A., and Takenaka, K. (2016). Thermoelectric properties of antiperovskite calcium oxides Ca_3PbO and Ca_3SnO. J. Appl. Phys. *119*, 205106. https://doi.org/10.1063/1.4952393.

39. Rani, U., Kamlesh, P.K., Shukla, A., and Verma, A.S. (2021). Emerging potential antiperovskite materials ANX_3 (A= P, As, Sb, Bi; X= Sr, Ca, Mg) for thermoelectric renewable energy generators. J. Solid State Chem. *300*, 122246. https://doi.org/10.1016/j.jssc.2021.122246.

40. Rani, U., Kamlesh, P.K., Agarwal, R., Kumari, J., and Verma, A.S. (2021). Electronic and thermo-physical properties of double antiperovskites X_6SOA_2 (X = Na, K and A = Cl, Br, I): A non-toxic and efficient energy storage materials. Int. J. Quant. Chem. *121*, e26759. https://doi.org/10.1002/qua.26759.

41. Gebhardt, J., and Rappe, A.M. (2017). Adding to the perovskite universe: inverse-hybrid perovskites. ACS Energy Lett. *2*, 2681–2685. https://doi.org/10.1021/acsenergylett.7b00966.

42. Wang, Y., Zhang, H., Zhu, J., Lü, X., Li, S., Zou, R., and Zhao, Y. (2020). Antiperovskites with exceptional functionalities. Adv. Mater. *32*, 1905007. https://doi.org/10.1002/adma.201905007.

43. Han, D., Feng, C., Du, M.-H., Zhang, T., Wang, S., Tang, G., Bein, T., and Ebert, H. (2021). Design of High-Performance Lead-Free Quaternary Antiperovskites for Photovoltaics via Ion Type Inversion and Anion Ordering. J. Am. Chem. Soc. *143*, 12369–12379. https://doi.org/10.1021/jacs.1c06403.

44. Han, D., Du, M.-H., Huang, M., Wang, S., Tang, G., Bein, T., and Ebert, H. (2022). Ground-state structures, electronic structure, transport properties and optical properties of Ca-based anti-Ruddlesden-Popper phase oxide perovskites. Phys. Rev. Mater. *6*, 114601. https://doi.org/10.1103/PhysRevMaterials.6.114601.

45. Rani, U., Soni, Y., Kamlesh, P.K., Pachori, S., and Verma, A.S. (2021). Fundamental theoretical design of Na-ion and K-ion based double antiperovskite X_6SOA_2 (X = Na, K; A = Cl, Br and I) halides: Potential candidate for energy storage and harvester. Int. J. Energy Res. *45*, 13442–13460. https://doi.org/10.1002/er.6673.

46. Kumar, A., Singh, S., Patel, A., Asokan, K., and Kanjilal, D. (2021). Thermoelectric properties of GaN with carrier concentration modulation: an experimental and theoretical investigation. Phys. Chem. Chem. Phys. *23*, 1601–1609. https://doi.org/10.1039/D0CP03950K.

47. Wang, H., Yu, L., Xu, J., Wei, D., Qin, G., Yao, Y., and Hu, M. (2021). Intrinsically low lattice thermal conductivity of monolayer hexagonal aluminum nitride (h-AlN) from first-principles: A comparative study with graphene. Int. J. Therm. Sci. *162*, 106772. https://doi.org/10.1016/j.ijthermalsci.2020.106772.

48. Yan, Y., Zhang, S., Ma, Q., Wang, Z., Feng, T., Chen, Q., Shi, B., Sun, F., Liang, M., Wang, J., et al. (2022). High power efficiency nitrides thermoelectric device. Nano Energy *101*, 107568. https://doi.org/10.1016/j.nanoen.2022.107568.

49. Pickard, C.J., and Needs, R.J. (2011). Ab initio random structure searching. J. Phys. Condens. Matter *23*. 053201. https://doi.org/10.1088/0953-8984/23/5/053201.

50. Pickard, C.J., and Needs, R.J. (2006). High-pressure phases of silane. Phys. Rev. Lett. *97*. 045504. https://doi.org/10.1103/PhysRevLett.97.045504.

51. Wang, Y., Lv, J., Zhu, L., and Ma, Y. (2012). CALYPSO: A method for crystal structure prediction. Comput. Phys. Commun. *183*, 2063–2070. https://doi.org/10.1016/j.cpc.2012.05.008.

52. Wang, Y., Lv, J., Zhu, L., and Ma, Y. (2010). Crystal structure prediction via particle-swarm optimization. Phys. Rev. B *82*. 094116. https://doi.org/10.1103/PhysRevB.82.094116.

53. Glazer, A.M. (1972). The classification of tilted octahedra in perovskites. Acta Crystallogr. B *28*, 3384–3392. https://doi.org/10.1107/S0567740872007976.

54. Howard, C.J., Kennedy, B.J., and Woodward, P.M. (2003). Ordered double perovskites–a group-theoretical analysis. Acta Crystallogr. B *59*, 463–471. https://doi.org/10.1107/S0108768103010073.

55. Born, M., Huang, K., and Lax, M. (1955). Dynamical theory of crystal lattices. Am. J. Phys. *23*, 474. https://doi.org/10.1119/1.1934059.

56. Jain, A., Shyue Ping, O., Hautier, G., Chen, W., Richards, W.D., Dacek, S., Cholia, S., Gunter, D., Skinner, D., Ceder, G., et al. (2013). Commentary: The Materials Project: A

Materials Genome Approach to Accelerating Materials Innovation. Apl. Mater. *1*. 011002. https://doi.org/10.1063/1.4812323.

57. Saal, J.E., Kirklin, S., Aykol, M., Meredig, B., and Wolverton, C. (2013). Materials design and discovery with high-throughput density functional theory: the open quantum materials database (OQMD). J. Miner. Met. Mater. Soc. *65*, 1501–1509. https://doi.org/10.1007/s11837-013-0755-4.

58. Curtarolo, S., Setyawan, W., Hart, G.L., Jahnatek, M., Chepulskii, R.V., Taylor, R.H., Wang, S., Xue, J., Yang, K., Levy, O., et al. (2012). AFLOW: An automatic framework for high-throughput materials discovery. Comput. Mater. Sci. *58*, 218–226. https://doi.org/10.1016/j.commatsci.2012.02.005.

59. Hadenfeldt, C., and Herdejürgen, H. (1988). Darstellung und Kristallstruktur der Calciumpnictidiodide Ca_2NI, Ca_2PI und Ca_2AsI. Z. Anorg. Allg. Chem. *558*, 35–40. https://doi.org/10.1002/zaac.19885580104.

60. Bailey, A.S., Hughes, R.W., Hubberstey, P., Ritter, C., Smith, R.I., and Gregory, D.H. (2011). New ternary and quaternary barium nitride halides; synthesis and crystal chemistry. Inorg. Chem. *50*, 9545–9553. https://doi.org/10.1021/ic201264u.

61. Liu, X., Wessel, C., Pan, F., and Dronskowski, R. (2013). Synthesis and single-crystal structure determination of the zinc nitride halides Zn_2NX (X= Cl, Br, I). J. Solid State Chem. *203*, 31–36. https://doi.org/10.1016/j.jssc.2013.03.046.

62. Skelton, J.M., Burton, L.A., Parker, S.C., Walsh, A., Kim, C.-E., Soon, A., Buckeridge, J., Sokol, A.A., Catlow, C.R.A., Togo, A., and Tanaka, I. (2016). Anharmonicity in the High-Temperature Cmcm Phase of SnSe: Soft Modes and Three-Phonon Interactions. Phys. Rev. Lett. *117*. 075502. https://doi.org/10.1103/PhysRevLett.117.075502.

63. Du, M.-H., and Singh, D.J. (2010). Enhanced Born charge and proximity to ferroelectricity in thallium halides. Phys. Rev. B *81*, 144114. https://doi.org/10.1103/PhysRevB.81.144114.

64. Poncé, S., Margine, E.R., and Giustino, F. (2018). Towards predictive many-body calculations of phonon-limited carrier mobilities in semiconductors. Phys. Rev. B *97*, 121201. https://doi.org/10.1103/PhysRevB.97.121201.

65. Noffsinger, J., Giustino, F., Malone, B.D., Park, C.-H., Louie, S.G., and Cohen, M.L. (2010). EPW: A program for calculating the electron–phonon coupling using maximally localized Wannier functions. Comput. Phys. Commun. *181*, 2140–2148. https://doi.org/10.1016/j.cpc.2010.08.027.

66. Ganose, A.M., Park, J., Faghaninia, A., Woods-Robinson, R., Persson, K.A., and Jain, A. (2021). Efficient calculation of carrier scattering rates from first principles. Nat. Commun. *12*, 2222. https://doi.org/10.1038/s41467-021-22440-5.

67. Flitcroft, J.M., Pallikara, I., and Skelton, J.M. (2022). Thermoelectric Properties of Pnma and Rocksalt SnS and SnSe. Solids *3*, 155–176. https://doi.org/10.3390/solids3010011.

68. Zhao, L.-D., Tan, G., Hao, S., He, J., Pei, Y., Chi, H., Wang, H., Gong, S., Xu, H., Dravid, V.P., et al. (2016). Ultrahigh power factor and thermoelectric performance in hole-doped single-crystal SnSe. Science *351*, 141–144. https://doi.org/10.1126/science.aad3749.

69. Kang, Y. (2023). Native point defects in antiperovskite Ba_3SbN: a promising semiconductor for photovoltaics. Phys. Chem. Chem. Phys. *25*, 9800–9806. https://doi.org/10.1039/d3cp00619k.

70. Dai, J., Ju, M.-G., Ma, L., and Zeng, X.C. (2019). Bi(Sb)NCa_3: Expansion of Perovskite Photovoltaics into All-Inorganic Anti-Perovskite Materials. J. Phys. Chem. C *123*, 6363–6369. https://doi.org/10.1021/acs.jpcc.8b11821.

71. Foster, S., and Neophytou, N. (2019). Doping optimization for the power factor of bipolar thermoelectric materials. J. Electron. Mater. *48*, 1889–1895. https://doi.org/10.1007/s11664-018-06857-1.

72. Wu, D., Zhao, L.-D., Tong, X., Li, W., Wu, L., Tan, Q., Pei, Y., Huang, L., Li, J.-F., Zhu, Y., et al. (2015). Superior thermoelectric performance in PbTe–PbS pseudo-binary: extremely low thermal conductivity and modulated carrier concentration. Energy Environ. Sci. *8*, 2056–2068. https://doi.org/10.1039/C5EE01147G.

73. Gong, J.J., Hong, A.J., Shuai, J., Li, L., Yan, Z.B., Ren, Z.F., and Liu, J.-M. (2016). Investigation of the bipolar effect in the thermoelectric material $CaMg_2Bi_2$ using a first-principles study. Phys. Chem. Chem. Phys. *18*, 16566–16574. https://doi.org/10.1039/C6CP02057G.

74. Wei, L., Chen, J.-f., He, Q.-y., and Teng, W. (2014). Study of lattice thermal conductivity of PbS. J. Alloys Compd. *584*, 381–384. https://doi.org/10.1016/j.jallcom.2013.09.081.

75. Togo, A., Chaput, L., and Tanaka, I. (2015). Distributions of phonon lifetimes in Brillouin zones. Phys. Rev. B *91*. 094306. https://doi.org/10.1103/PhysRevB.91.094306.

76. Chaput, L. (2013). Direct solution to the linearized phonon Boltzmann equation. Phys. Rev. Lett. *110*, 265506. https://doi.org/10.1103/PhysRevLett.110.265506.

77. Lindsay, L., and Broido, D.A. (2011). Enhanced thermal conductivity and isotope effect in single-layer hexagonal boron nitride. Phys. Rev. B *84*, 155421. https://doi.org/10.1103/PhysRevB.84.155421.

78. Singh, D., Murthy, J.Y., and Fisher, T.S. (2011). Mechanism of thermal conductivity reduction in few-layer graphene. J. Appl. Phys. *110*. 044317. https://doi.org/10.1063/1.3622300.

79. Fugallo, G., Cepellotti, A., Paulatto, L., Lazzeri, M., Marzari, N., and Mauri, F. (2014). Thermal conductivity of graphene and graphite: collective excitations and mean free paths. Nano Lett. *14*, 6109–6114. https://doi.org/10.1021/nl502059f.

80. Palenzona, A., Manfrinetti, P., and Fornasini, M.L. (2000). Phase diagram of the Ca–Sn system. J. Alloys Compd. *312*, 165–171. https://doi.org/10.1016/S0925-8388(00)01150-6.

81. Rahim, W., Skelton, J.M., and Scanlon, D.O. (2021). Ca_4Sb_2O and Ca_4Bi_2O: two promising mixed-anion thermoelectrics. J. Mater. Chem. A *9*, 20417–20435. https://doi.org/10.1039/D1TA03649A.

82. Whalley, L.D., Skelton, J.M., Frost, J.M., and Walsh, A. (2016). Phonon anharmonicity, lifetimes, and thermal transport in $CH_3NH_3PbI_3$ from many-body perturbation theory. Phys. Rev. B *94*, 220301. https://doi.org/10.1103/PhysRevB.94.220301.

83. Khazaei, M., Wang, J., Estili, M., Ranjbar, A., Suehara, S., Arai, M., Esfarjani, K., and Yunoki, S. (2019). Novel MAB phases and insights into their exfoliation into 2D MBenes. Nanoscale *11*, 11305–11314. https://doi.org/10.1039/C9NR01267B.

84. He, X., Zhang, H., Nose, T., Katase, T., Tadano, T., Ide, K., Ueda, S., Hiramatsu, H., Hosono, H., and Kamiya, T. (2022). Degenerated Hole Doping and Ultra-Low Lattice Thermal Conductivity in Polycrystalline SnSe by Nonequilibrium Isovalent Te Substitution. Adv. Sci. *9*, 2105958. https://doi.org/10.1002/advs.202105958.

85. Sun, J., Zhang, C., Yang, Z., Shen, Y., Hu, M., and Wang, Q. (2022). Four-phonon scattering effect and two-channel thermal transport in two-dimensional paraelectric SnSe. ACS Appl. Mater. Interfaces *14*, 11493–11499. https://doi.org/10.1021/acsami.1c24488.

86. Ioffe, A.F. (1960). Physics of Semiconductors (Infosearch).

87. Shao, H., Tan, X., Liu, G.-Q., Jiang, J., and Jiang, H. (2016). A first-principles study on the phonon transport in layered BiCuOSe. Sci. Rep. *6*, 21035–21039. https://doi.org/10.1038/srep21035.

88. Clark, S.J., Segall, M.D., Pickard, C.J., Hasnip, P.J., Probert, M.I.J., Refson, K., and Payne, M.C. (2005). First principles methods using CASTEP. Z. für Kristallogr. - Cryst. Mater. *220*, 567–570. https://doi.org/10.1524/zkri.220.5.567.65075.

89. Kresse, G., and Furthmüller, J. (1996). Efficient iterative schemes for ab initio total-energy calculations using a plane-wave basis set. Phys. Rev. B *54*, 11169–11186. https://doi.org/10.1103/PhysRevB.54.11169.

90. Perdew, J.P., Burke, K., and Ernzerhof, M. (1996). Generalized gradient approximation made simple. Phys. Rev. Lett. *77*, 3865–3868. https://doi.org/10.1103/PhysRevLett.77.3865.

91. Heyd, J., Scuseria, G.E., and Ernzerhof, M. (2003). Hybrid functionals based on a screened coulomb potential. J. Chem. Phys. *118*, 8207–8215. https://doi.org/10.1063/1.1564060.

92. M Ganose, A., J Jackson, A., and O Scanlon, D. (2018). sumo: Command-line tools for plotting and analysis of periodic ab initio calculations. J. Open Source Softw. *3*, 717. https://doi.org/10.21105/joss.00717.

93. Togo, A., and Tanaka, I. (2015). First principles phonon calculations in materials science. Scripta Mater. *108*, 1–5. https://doi.org/10.1016/j.scriptamat.2015.07.021.

94. Poncé, S., Li, W., Reichardt, S., and Giustino, F. (2020). First-principles calculations of charge carrier mobility and conductivity in bulk semiconductors and two-dimensional materials. Rep. Prog. Phys. *83*. 036501. https://doi.org/10.1088/1361-6633/ab6a43.

95. Baroni, S., De Gironcoli, S., Dal Corso, A., and Giannozzi, P. (2001). Phonons and related crystal properties from density-functional perturbation theory. Rev. Mod. Phys. *73*, 515–562. https://doi.org/10.1103/RevModPhys.73.515.

96. Wang, S., Huang, M., Wu, Y.N., and Chen, S. (2021). Absolute Volume Deformation Potentials of Inorganic ABX_3 Halide Perovskites: The Chemical Trends. Adv. Theory Simul. *4*, 2100060. https://doi.org/10.1002/adts.202100060.

97. McGaughey, A.J.H., and Kaviany, M. (2004). Quantitative validation of the Boltzmann transport equation phonon thermal conductivity model under the single-mode relaxation time approximation. Phys. Rev. B *69*. 094303. https://doi.org/10.1103/PhysRevB.69.094303.

98. Eriksson, F., Fransson, E., and Erhart, P. (2019). The hiphive package for the extraction of high-order force constants by machine learning. Adv. Theory Simul. *2*, 1800184. https://doi.org/10.1002/adts.201800184.

99. Brorsson, J., Hashemi, A., Fan, Z., Fransson, E., Eriksson, F., Ala-Nissila, T., Krasheninnikov, A.V., Komsa, H.P., and Erhart, P. (2022). Efficient Calculation of the Lattice Thermal Conductivity by Atomistic Simulations with Ab Initio Accuracy. Adv. Theory Simul. *5*, 2100217. https://doi.org/10.1002/adts.202100217.

100. Spooner, K.B., Einhorn, M., Davies, D.W., and Scanlon, D.O.. ThermoParser. https://github.com/SMTG-Bham/ThermoParser.

101. Brlec, K., Spooner, K.B., Skelton, J.M., and Scanlon, D.O. (2022). $Y_2Ti_2O_5S_2$ – a promising n-type oxysulphide for thermoelectric applications. J. Mater. Chem. A *10*, 16813–16824. https://doi.org/10.1039/D2TA04160J.

102. Spooner, K.B., Ganose, A.M., Leung, W.W.W., Buckeridge, J., Williamson, B.A.D., Palgrave, R.G., and Scanlon, D.O. (2021). $BaBi_2O_6$: A Promising n-Type Thermoelectric Oxide with the $PbSb_2O_6$ Crystal Structure. Chem. Mater. *33*, 7441–7456. https://doi.org/10.1021/acs.chemmater.1c02164.